IOP Publishing Supercond. Sci. Technol. 39 (2026) 035005 https://doi.org/10.1088/1361-6668/ae496a

Superconductor Science and Technology

PAPER

Preparation of the Cu-based Nb_3Sn sample via bronze route for quadrupole resonator testing

Ming Lu[1,2,*], **Sebastian Keckert**[1], **Felix Kramer**[1], **Alena Prudnikava**[1], **Jens Knobloch**[1,3], **Aleksandr Zubtsovskii**[3] and **Oliver Kugeler**[1]

[1] Helmholtz-Zentrum Berlin für Materialien und Energie GmbH, 14109 Berlin, Germany
[2] Institute of Modern Physics, Chinese Academy of Sciences, Lanzhou 730000, People's Republic of China
[3] Universität Siegen, 57076 Siegen, Germany
[*] Author to whom any correspondence should be addressed.

E-mail: ming.lu@helmholtz-berlin.de

Keywords: Nb_3Sn, bronze route, Cu substrate, QPR, surface resistance, SRF

Supplementary material for this article is available online

OPEN ACCESS

RECEIVED
1 October 2025

REVISED
4 February 2026

ACCEPTED FOR PUBLICATION
23 February 2026

PUBLISHED
6 March 2026

Abstract

We report the successful production of a Cu-based Nb_3Sn sample specifically designed for quadrupole resonator (QPR) testing, representing a significant step toward scalable radio-frequency superconducting coatings of Nb_3Sn on copper substrates. The sample was fabricated using an optimized electrochemical thermal synthesis via bronze route, incorporating several key advancements: electropolishing of the Cu substrate, electroplating of the bronze precursor layer, a tailored heat treatment at 700 °C to promote grain growth and suppress tin-rich secondary phases, and a newly developed chemical etching procedure for effective removal of surface bronze residues and contaminants. These improvements address longstanding challenges in the fabrication of high-quality Cu-based Nb_3Sn thin films. Subsequent QPR measurements yielded the peak magnetic field and temperature dependent surface resistance R_s, as well as the superconducting transition temperature and quench field. The achieved surface resistance, with a minimum of 47.5 nΩ at 4.5 K and 15 mT (413 MHz), indicates that both residual and BCS losses contribute significantly to the present performance limitations. This behavior is consistent with the observed sub-stoichiometric composition and microstructural inhomogeneity of the film. Although the procedure is not yet fully optimized the results clearly demonstrate the feasibility of this approach and its potential for further improvement through process refinement.

1. Introduction

Nb_3Sn has emerged as a promising material for next-generation superconducting radio-frequency (SRF) cavities due to its high critical temperature ($T_c \approx 18$ K) and intrinsically low BCS surface resistance—the temperature-dependent component of radio-frequency (RF) losses arising from thermally excited quasiparticles—which enables efficient operation at 4.2 K and significantly reduces cryogenic complexity and cost [1, 2]. Significant progress has been achieved using tin vapor diffusion to coat Nb substrates with Nb_3Sn, yielding RF performance characterized by a lower surface resistance ($<20\,n\Omega$) than bulk Nb at 4.2 K and moderate accelerating fields [3, 4]. In recent years, Sun *et al* [5] in Cornell developed a Cu-free electroplating process on Nb surfaces. The authors demonstrated ultra-low BCS surface resistances notably lower than vapor-diffused cavities. Nevertheless, both of these approaches require high-temperature treatments above 1000 °C, which makes them unsuitable for Cu substrates. Currently, extending Nb_3Sn coatings to Cu substrates—an attractive alternative due to Cu's superior thermal conductivity, mechanical properties, and lower cost—remains a considerable challenge [6].

Cu-based SRF cavities offer compelling advantages, particularly through their compatibility with cryocooler-based conduction cooling [7, 8]. The high thermal conductivity of Cu facilitates efficient heat

extraction, potentially eliminating the need for liquid helium and enabling operation at elevated temperatures (4.2–4.5 K). Such configurations are highly desirable for compact accelerators in industrial, medical, and space environments [9]. However, synthesizing high-quality, low-loss Nb_3Sn films on Cu substrates has been hindered by several issues, including a loose and porous microstructure of the Nb_3Sn layer, poor interfacial adhesion, film cracking induced by thermal expansion mismatch, and the formation of non-stoichiometric or performance-degrading phases [6, 10].

Various thin-film fabrication techniques have been explored for Cu-based Nb_3Sn, such as tin vapor diffusion combined with outer-wall copper coating [11], magnetron sputtering [6, 12], chemical vapor deposition [13], and the bronze route [14, 15]. Among these, the bronze route—originally developed for multifilamentary wire fabrication [16]—has gained renewed attention due to its relatively low synthesis temperature (∼700 °C), which makes it compatible with Cu substrates. The bronze route to produce Nb_3Sn is a well-established process in superconducting wires for decades (DC application). Non-superconducting phases and Cu related inclusions are observed, while these can be tolerated in DC applications (although the resulting critical current density J_c is not outstanding), such materials are still on the market [17].

In its thin-film RF applications, Barzi *et al* [18] first attempted to leverage their experience from wire development and published a Cu/Sn/Cu/Nb stack (literally a bronze route), noting Cu-related inclusions and highlighting the associated challenges. Later, KEK groups Ito *et al* [19] attempted both Cu/Sn/Cu/Nb stacks and bronze processes and reported similar issues. Clearly, the bronze-route process has long faced fundamental challenges, such as Cu-related inclusions, surface bronze residues and tin-rich secondary phases, which may hinder successful RF applications and have led to stagnation in related research for years.

However, the atom probe tomography measurements by Sandim *et al* [20] revealed that Cu-related inclusions are primarily located at grain boundaries, with extremely low solubility inside Nb_3Sn grains. This conclusion is consistent with the later cross-sectional energy-dispersive x-ray spectroscopy (EDX) analyzes by Withanage *et al* [14], which reported negligible Cu content within the Nb_3Sn coating itself. In 2022, the IMP group reported vertical tests of 1.3 GHz Nb_3Sn cavities prepared via the bronze route, demonstrating that the achieved Q_0 surpassed that of bulk Nb cavities measured at 4.2 K [21] ($Q_0 = 1.2 \times 10^9$ at $E_{acc} = 2\,\mathrm{MV\,m^{-1}}$). Further studies by this group in 2025 showed that, after optimization of the chemical etching formulation, the Cu-related inclusions were further reduced. Meanwhile, tin-rich secondary phases were converted into the Nb_3Sn phase by optimizing the tin content of the bronze precursor and heat-treatment configuration [22], indicating that the bronze route process may be feasible for certain sample sizes and performance tolerances.

Applying the bronze route to Cu substrates involves many challenges that need to be addressed. Cu inclusions in thin films can form normal-conducting regions, which degrade RF performance by increasing surface resistance and inducing premature quenching [6, 14]. Residual bronze, Sn-rich secondary phases (e.g. Nb_6Sn_5, $NbSn_2$), and oxygen-related compounds such as Nb oxides (NbO_x) and Sn oxides (SnO_2) further exacerbate RF losses and limit field stability [22]. Moreover, thermal strain arising from the mismatch in thermal expansion coefficients between Nb_3Sn and Cu can induce microcracks within the film or along grain boundaries, but also locally suppress the superconducting transition temperature T_c, thereby further deteriorating the overall superconducting properties [16]. These challenges demand careful control of plating, annealing, and post-treatment to achieve uniform and defect-free Nb_3Sn coatings on Cu substrates.

Within this established research path, the present work aim to extend bronze-route to a Nb/Cu substrate and to provide a quantitative quadrupole resonator (QPR)-based RF characterization of the resulting Cu-based Nb_3Sn coating. We position our contribution as a step towards assessing what level of RF performance can realistically be achieved with such coatings on Cu, and which limitations must still be addressed in future iterations of the process. Overall, the bronze-route Nb_3Sn/Cu system remains fundamentally limited today by incomplete A15 formation, Sn inhomogeneity, and a quench field far below the theoretical limit, and its near-term progress must therefore be viewed as incremental rather than transformative.

In concrete terms, the present study advances the field in three ways. First, it provides the first quantitative QPR-based RF characterization of a bronze-route Nb_3Sn coating grown on a Nb/Cu substrate, thereby establishing an experimental benchmark that did not previously exist for this materials system. Second, by correlating RF performance with detailed microscopy, magnetization and penetration-depth measurements, the work clarifies which microstructural features (Sn-rich phases, Cu-assisted ntermetallics, strain gradients) most strongly limit quench field and T_c. Third, the study demonstrates an electrochemical–thermal synthesis (ETS) route compatible with conduction-cooled cryomodule concepts, providing a realistic pathway for future optimization.

2. Sample preparation and experimental methods

2.1. Overview

This outlines the complete fabrication route and characterization methodology employed for producing Nb_3Sn thin films on Cu substrates using the ETS method. It involves sequential deposition of a Nb diffusion barrier and a bronze precursor layer, followed by annealing to promote solid-state Nb_3Sn formation [18, 21]. The multi-step procedure—schematically illustrated in figure 1—includes Cu substrate surface preparation, deposition of the Nb barrier layer, electroplating of the bronze precursor, heat treatment for Nb_3Sn phase formation, and final chemical etching to remove top impurity layer.

Initial attempts revealed that the resulting Nb_3Sn films exhibited non-uniform coverage, with localized uncoated regions appearing as large pits (1–3 mm in diameter) visible to the naked eye and smaller voids of several tens of micrometers revealed by laser scanning microscopy (LSM). These defects were suspected to originate from air bubbles trapped on the surface during the immersion of the inverted QPR sample into the bronze plating solution, which inhibited uniform bronze deposition. To address this issue, a repair procedure was implemented. The sample surface was activated using Citranox® to enhance hydrophilicity, and after the electrolyte was stabilized, it was re-immersed into the electroplating bath at a tilted angle to minimize bubble adhesion. A new bronze layer was deposited, followed by repeated heat treatment and chemical etching. This improved process resulted in a more uniform and continuous Nb_3Sn coating over the entire plated region of the QPR sample (with a top diameter of about 7.5 cm).

A detailed description of each fabrication step, along with its intended purpose, is summarized in table 1. It should be noted that steps 7–10 were repeated twice for this QPR sample due to repair experiment. The process begins with mechanical and electrochemical polishing to ensure a clean and smooth Cu surface. A dense Nb layer with a thickness of about 10 μm is subsequently sputtered onto the substrate, serving both as a reactive layer for Nb_3Sn formation and as a diffusion barrier to prevent interdiffusion between Cu and Nb_3Sn. This Nb layer must possess high density and sufficient thickness to prevent the Nb_3Sn film from degrading. So, the Nb film was then annealed at 700 ° for 20 h to promote grain growth, enhance film density and relieve internal stress. It is then followed by the electroplating of a top bronze precursor layer. Controlled annealing with a slow ramp-up to 700 ° and holding for 30 h promotes solid-state diffusion to form the Nb_3Sn superconducting phase. Post-treatments, including aqua regia etching and ultrapure water rinsing, remove residual surface bronze impurities, and contaminants.

To evaluate the RF performance of Nb_3Sn films, we employ the QPR developed at Helmholtz-Zentrum Berlin (HZB), a highly sensitive diagnostic tool designed for thin–film characterization under controlled frequency, temperature, and RF–field conditions (the QPR concept was originally developed at CERN [23, 24] and subsequently optimised at HZB [25, 26]). The QPR measures the surface resistance of the sample using a calorimetric method, achieving an accuracy in the sub–nanoohm range. By analyzing R_s as a function of temperature, the BCS and residual components of the surface resistance can be extracted via fitting procedures. The measurement uncertainty of R_s is estimated to be below 5% [26].

This approach facilitates sensitive and accurate characterization of RF losses in superconducting films under various operational conditions. Operating at 415, 850, and 1285 MHz, the QPR allows direct assessment of frequency-dependent RF losses [27, 28]. Its mechanical stability and precise thermal control down to 1.9 K ensure high measurement reproducibility. The QPR features a field distribution that includes both electric and magnetic components, closely resembling the conditions in real accelerator cavities.

Besides the calorimetric measurements of R_s, the QPR also allows to study the penetration depth $\lambda(T)$ by measuring the shift of resonant frequency as a function of sample temperature. The RF quench field B_{max} of the sample is obtained by applying single RF pulses to the cavity and recording the RF pulse traces with fast peak power meters. For more details about the measurement techniques the reader is referred to [27]. Some peculiarities of the quench field measurement that is specific to this publication can be found in the Supplementary Material. The insights gained with the QPR provide essential feedback for establishing the relationship between microstructural features and RF performance, thereby guiding the further refinement of Nb_3Sn thin-film fabrication techniques.

2.2. Substrate preparation

The Cu QPR sample used in this study was a monolithic, weld-free structure directly machined from high-purity oxygen-free high-conductivity Cu (top diameter: 75 mm; height: 100 mm), with dimensions compatible with standard QPR testing requirements [27]. To ensure a clean and smooth surface suitable

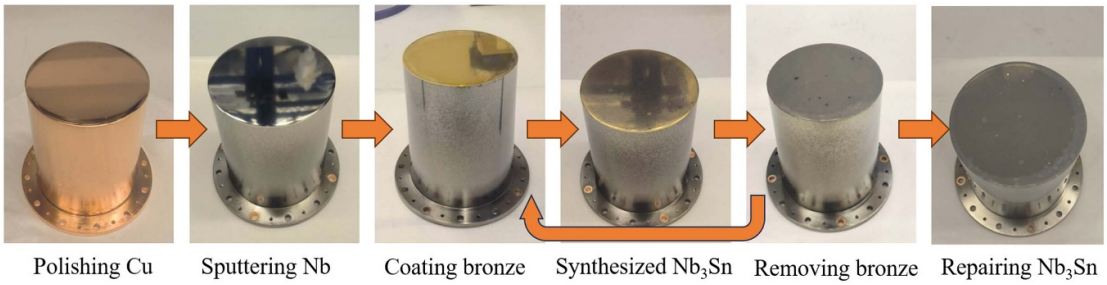

Figure 1. Flowchart of the preparation procedure for the Cu-based Nb_3Sn sample.

Table 1. Fabrication procedure of the Cu-based Nb_3Sn sample.

Step	Process description	Purpose
1	Mechanical polishing to 100 μm	Removal of surface damage and reduction of defects
2	Degreasing with 1% Citranox® for 1 h	Eliminate organic contaminants and grease
3	Electro-polishing (EP) 30 μm	Achieve a smooth surface with reduced roughness
4	Rinse with ultrapure water	Remove residual acids and particles
5	Sputtering of 10 μm Nb layer by HiPIMS	Deposit a superconducting Nb barrier layer
6	High-temperature annealing at 700 °C for 20 h	Enhance film density and relieve internal stress
7	Electroplating of 10 μm bronze layer	Deposit bronze precursor layer for Nb_3Sn formation
8	Heat treatment at 700 °C for 30 h	Form Nb_3Sn via solid-state diffusion reaction
9	Removal of surface bronze using aqua regia	Expose Nb_3Sn layer and remove residual impurities
10	Final rinse with ultrapure water	Ensure clean, residue-free surface for RF testing

for thin-film deposition, the sample was mechanically polished using SiC sandpapers of progressively finer grit sizes (#180, #300, #500, #800, #1200, #2000, and #5000) to remove approximately 100 μm of material.

Subsequently, EP was employed to further improve surface quality, removing an additional ~30 μm. To optimize the polishing uniformity, a COMSOL Multiphysics simulation was performed to analyze the thickness distribution under various electrode arrangements conditions. The simulation used the 'Tertiary Current Distribution' interface, assuming Tafel kinetics at the anode and cathode surfaces, with exchange current densities of 10 A m^2 and anodic/cathodic transfer coefficients of 0.5, consistent with typical values reported for copper electropolishing in phosphoric acid–butanol electrolytes [29]. Based on the simulation results (figure 2), a custom-designed vertical support fixture was fabricated from chemically resistant polytetrafluoroethylene and polyether ether ketone to achieve uniform material removal. The fixture allowed precise positioning of the Cu substrate (anode) at the bottom, while disc- and strip-shaped Cu cathodes were symmetrically arranged above and around it. An optimized anode–cathode spacing of 10 mm—corresponding to the distance between the Cu anode surface and the upper disc cathode—was determined from COMSOL simulations and preliminary tests to provide uniform current distribution and minimize edge effects.

Electropolishing was carried out at room temperature (20 °C) using an electrolyte composed of phosphoric acid (85 wt%) and 1-Butanol (>99 wt%) in a 3:2 volume ratio. The slow-scan linear sweep voltammetry (LSV) measurements provided insights into the electropolished Cu process. (See in figure 6(a)) A constant voltage of 2.1 V was applied for 2 h under magnetic stirring at 100 rpm. After polishing, the sample was thoroughly rinsed with deionized (DI) water and dried in a nitrogen atmosphere. The resulting surface exhibited a uniform, mirror-like Cu luster, indicating high polishing quality.

Surface morphology and roughness were characterized using LSM. As shown in figure 3, the polished surface exhibits an overall smooth appearance with mean surface roughness (Sa) of approximately 97.3 nm measured over an area of 250 μm × 250 μm. However, a significant number of micro-scale surface pits are observed, with typical diameters of several micrometers and depths less than 1 μm. These defects are suspected to originate from oxygen-bubble formation on the surface during the EP process, which disrupts uniform dissolution. Although the current surface quality meets the basic requirements for thin-film deposition, these surface pits remain a challenge and may adversely affect the coating uniformity. Efforts are ongoing to optimize the EP process parameters and fixture design to mitigate this issue.

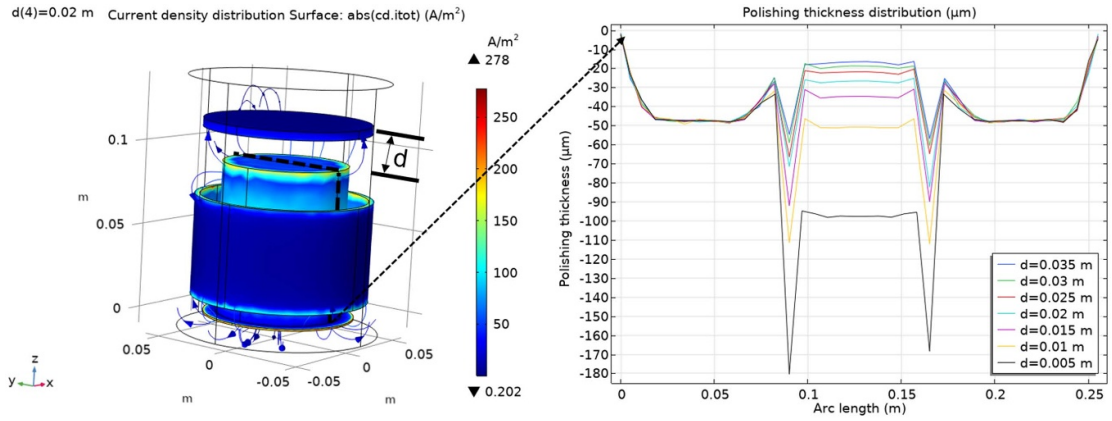

Figure 2. COMSOL Multiphysics simulation of the Cu material removal during electrochemical polishing of the QPR sample, showing improved uniformity with minor edge effects influenced by electrode geometry and electrolyte dynamics. The distance d refers to the spacing between the Nb cathode and the upper disc anode.

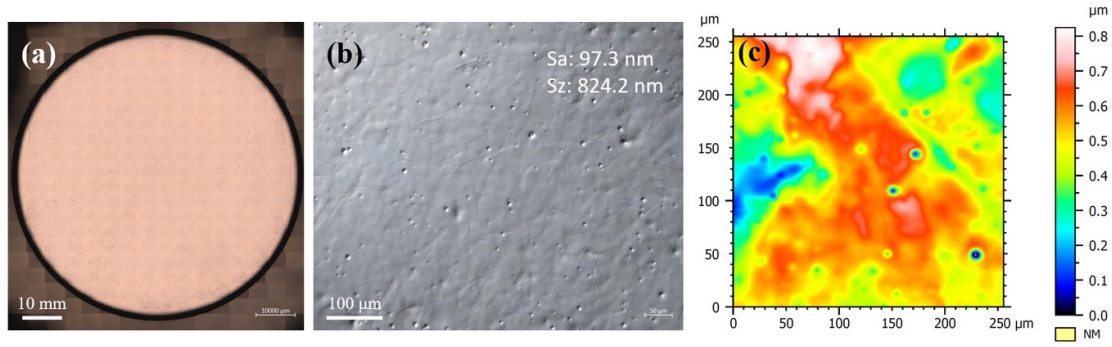

Figure 3. Surface images of the Cu substrate after electrochemical polishing: (a) bright-field optical microscope image with a 10 mm scale, (b) dark-field optical microscope image with a 100 μm scale, and (c) LSM topography over a 250 $\times$ 250 μm^2 area, showing a smooth surface with an average roughness of 97.3 nm and some pitting defects.

2.3. Nb reaction layer deposition

The Nb film, serving as both a diffusion barrier and a precursor for subsequent Nb_3Sn formation, was deposited on the outer surface of the Cu QPR sample using high-power impulse magnetron sputtering (HiPIMS) in a commercial, high-volume, fully automated coating system (CemeCon CC800). Prior to deposition, the entire coating chamber, including the QPR sample, was baked at approximately 300 °C for 6 h and then cooled down to the coating temperature. The deposition was carried out at a substrate temperature of approximately 180 °C in an argon (Ar) atmosphere with a working pressure of 0.02 mbar and an Ar flow rate of 700 sccm. A high-purity Nb target (99.99%) was powered with an average cathode power of 600 W (equivalent to 6.8 W cm^{-2}), using a HiPIMS pulsed power supply operating at 1000 Hz with a pulse width of 100 μs. A constant substrate bias of -50 V was applied. The base pressure prior to sputtering was maintained below 7×10^{-7} mbar, which is sufficient to minimize contamination during Nb deposition. Indeed, high-quality Nb thin films deposited under similar conditions using the same CemeCon sputtering system have been reported [30].

To improve coating uniformity on the curved sidewalls and bottom regions of the sample, the Cu QPR sample was mounted on a custom tiltable holder that oscillated within a $\pm 15°$ angular range during deposition. This dynamic motion enhanced angular coverage and produced a Nb film with a thickness of approximately 10 μm on the top surface, as monitored *in situ* by a quartz crystal microbalance during deposition and verified from prior cross-sectional LSM measurements on reference samples. The thickness error measured by both methods does not exceed 10%. However, due to geometric shadowing and the inherently directional nature of sputtering, the film thickness gradually decreased along the vertical sidewalls, falling below 1 μm near the bottom edge. In this region Nb_3Sn synthesis does not take place, and it is essential to ensure that the cylinder remains superconducting. Since the RF field is very low in this cylinder region and thickness is still far more than the Nb penetration depth.

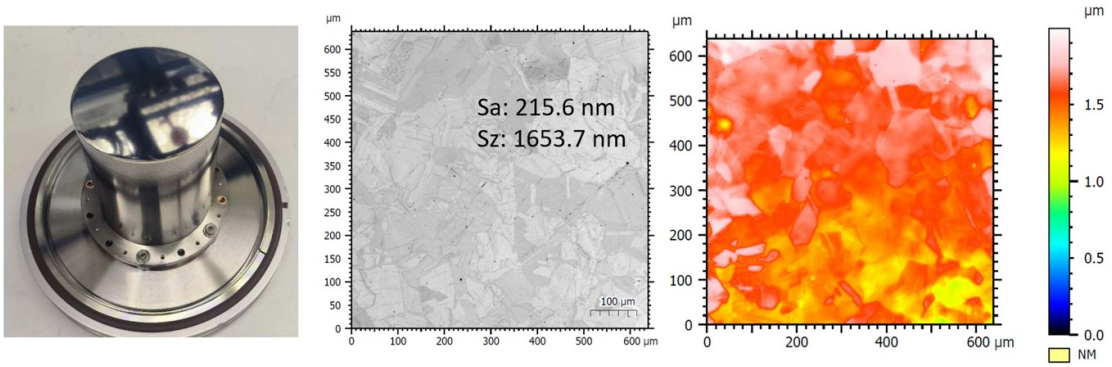

Figure 4. LSM image of the Nb reaction layer surface, showing a smooth, uniform morphology free of cracks.

Table 2. Composition of the bronze electroplating solution [31].

Chemical	Formula	Purity	Vendor	Concentration ($g\,L^{-1}$)
Citric acid	$C_6H_8O_7$	AR, 99.5%	Merck	180
Potassium stannate	K_2SnO_3	AR, 95.0%	Alfa Aesar	20
Basic copper carbonate	$Cu_2(OH)_2CO_3$	AR	Merck	16
Potassium hydroxide	KOH	AR, 99.5%	Merck	130
Monopotassium phosphate	KH_2PO_4	AR	Alfa Aesar	17

Surface morphology and roughness of the deposited Nb film were characterized using LSM. The analysis confirmed a significant reduction in surface pitting compared to the underlying Cu substrate, revealing a continuous and crack-free Nb layer with no visible contamination. As shown in figure 4, the Nb film exhibits a relatively uniform surface morphology with Sa of approximately 215.6 nm measured over an area of 600 μm × 600 μm. This level of smoothness is considered suitable for the subsequent Nb_3Sn formation.

2.4. Bronze electroplating

Bronze electroplating offers several advantages, including low cost, excellent scalability for batch production, and strong adaptability to complex cavity geometries. Moreover, the process parameters—such as layer composition, thickness, and annealing conditions—can be precisely controlled, enabling reproducible Nb_3Sn film properties.

An electroplated bronze precursor layer (Sn content ∼10 at.%), serving as the tin source for Nb_3Sn formation, was deposited on the Nb-coated top surface of the QPR sample using an alkaline citrate-based electrolyte. The composition of the plating solution is listed in table 2. The Nb film on the side and bottom surfaces of the sample is relatively thin, which could lead to local copper exposure during the bronze-route Nb_3Sn coating process. Such exposed copper would result in excessive RF losses and obscure the intrinsic surface resistance R_s of the Nb_3Sn layer. To mitigate this issue, the Nb_3Sn coating was applied only to the top surface, while the Nb film on the sides and bottom was left unchanged. This selective coating does not significantly affect the calorimetric surface-resistance measurement, as the RF field is concentrated on the top surface and decays exponentially along the side walls.

Similar to the optimization of the EP process, a detailed simulation of electroplating process and the bronze deposition thickness distribution was conducted using COMSOL Multiphysics to optimize the electrode configuration and masking strategy. The simulation results, shown in figure 5, the horizontal axis (‘arc length’) corresponds to the line-scan distance along the black dashed line indicated on the QPR sample surface. The inset illustrates the relative spatial arrangement of the QPR sample and the copper anode, where the bottom orange circle represents the anode. Besides, the simulation employed the Tertiary Current Distribution interface, with Tafel kinetics applied at both the anode (bronze electrode) and the cathode (QPR sample) surfaces. Exchange current densities were set to 10 $A\,m^{-2}$, and both anodic and cathodic transfer coefficients were assumed to be 0.5. The electrolyte was modeled with uniform conductivity, and convection effects were included to account for ion transport and concentration gradients. The primary objective of the simulation was to achieve uniform bronze deposition on the

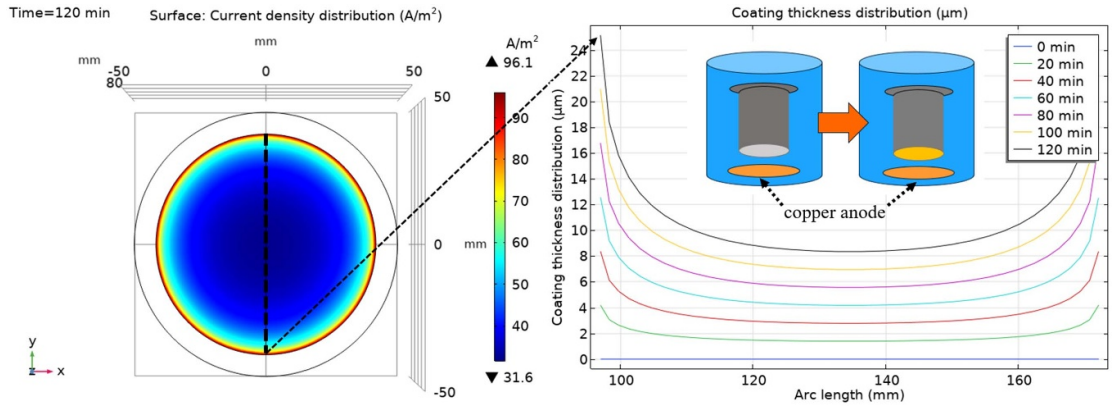

Figure 5. COMSOL simulation of the bronze electroplating thickness distribution on the QPR sample, showing the influence of masking strategy, sample orientation, and electrode geometry on coating uniformity.

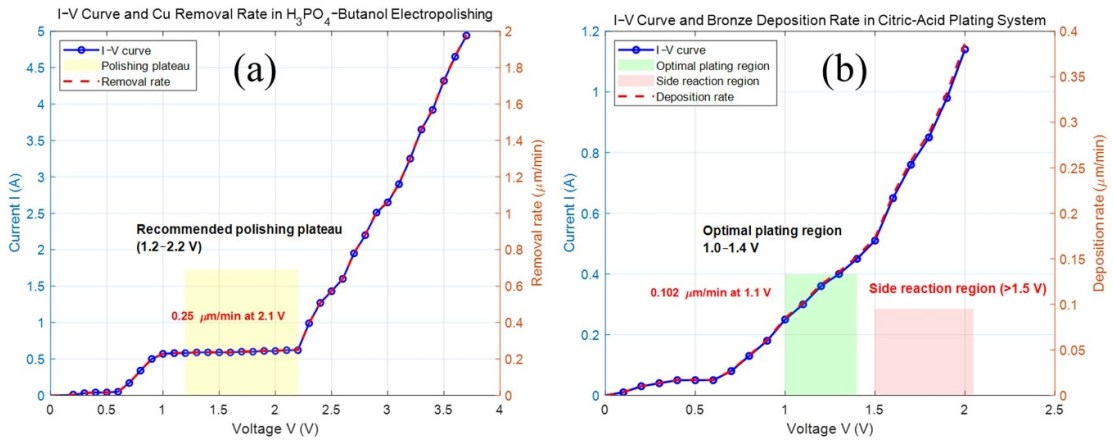

Figure 6. Slow-scan linear sweep voltammograms (LSV) of (a) electropolished Cu and (b) electrodeposited Cu–Sn alloy (bronze) under the applied plating conditions. The curves illustrate the electrochemical behavior of the Cu substrate and the co-deposition process of Cu–Sn, providing insight into the deposition kinetics.

top surface of the QPR sample by optimizing the electrode geometry, spacing, and masking design. To prevent unwanted deposition, the sidewalls and bottom surface—where the niobium barrier layer (below 1 μm) was insufficiently thick—were isolated from the electrolyte during the plating process.

Based on the simulation insights, the QPR sample was mounted upside down with its top surface partially immersed in the electrolyte. The sidewalls and bottom were masked with chemically resistant tape to block deposition in these areas. A horizontal Cu anode disk was positioned directly below the sample 20 mm to provide uniform current distribution and minimize anode sludge contamination. Representative electrochemical characterization was performed to verify the stability of the bronze deposition process. The slow-scan LSV measurements provided insights into the Cu–Sn co-deposition process. As shown in figure 6 (b), typical parameters included a current density of 5 mA cm^{-2}, a citrate-based electrolyte with 10 at.% Sn content, and deposition at room temperature. Although detailed bath composition and additive concentrations are proprietary, the electrochemical behavior is consistent with conventional citrate-based bronze electroplating systems reported in the literature [14, 32]. Electroplating was performed in galvanostatic mode at a constant current density of 5 mA cm^{-2} for 2 h, at a bath temperature of 20 °C. This process yielded a bronze layer of approximately 10 μm on the top surface.

After plating, the sample was rinsed with ultrapure water and dried under a nitrogen stream. The surface morphology and roughness of the bronze layer were examined using LSM. As shown in figure 7, the bronze coating exhibited a uniform and crack-free morphology with no apparent particulate contamination, indicating the effectiveness of the optimized electroplating setup. The measured arithmetic Sa was 196.6 nm measured over an area of 600 μm × 600 μm, which is acceptable for the subsequent

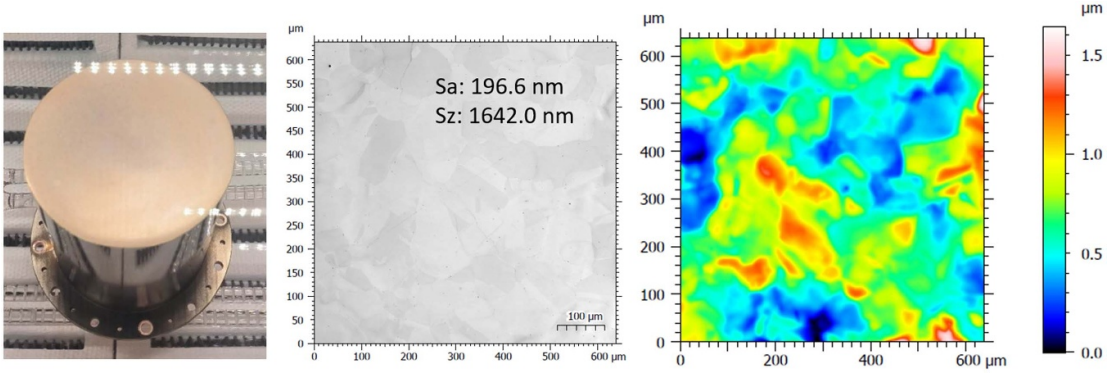

Figure 7. LSM image of the bronze-coated surface on the Nb-coated QPR sample. The surface shows a smooth, uniform morphology with no visible cracks or contamination.

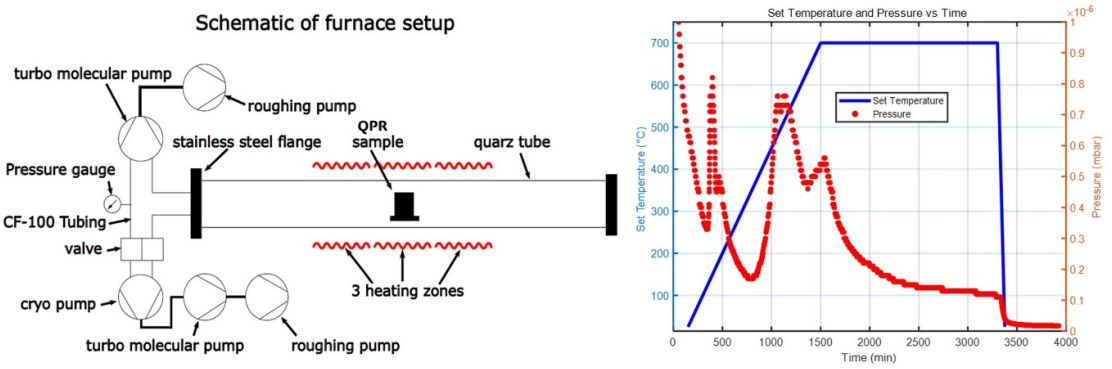

Figure 8. Schematic of the horizontal three-zone KVZ 12/1200 furnace with the pumping system, and a plot of the programmed set temperature and measured chamber pressure versus time during Nb_3Sn heat treatment.

Nb_3Sn coating. Interestingly, after bronze electroplating, the Sa decreased while the Sz remained essentially unchanged compared with the previous Nb sputtering step. This can be explained by the deposition of bronze into micro-scale depressions, which reduces the overall average roughness, whereas the extreme surface peaks and valleys remain largely unaffected.

2.5. Heat treatment for Nb_3Sn synthesis

All heat treatments were conducted in a horizontal three-zone KVZ 12/1200 tube furnace with a maximum operating temperature of 1200 °C and a total heated length of 1200 mm. A 150 mm diameter quartz tube served as the reaction chamber, and the samples were placed at the center of the uniform-temperature zone. The furnace was evacuated using a combination of a dry scroll pump, a turbomolecular pump, and a cryopump. A base pressure of approximately 5×10^{-7} mbar was reached prior to the main heat-up phase, and the pressure at 700 °C was maintained below 5×10^{-7} mbar. Figure 8 shows a schematic of the horizontal three-zone KVZ 12/1200 furnace with the pumping system, as well as the programmed temperature profile and the measured pressure variation during a representative Nb_3Sn heat treatment process.

Multilayer bronze/Nb/Cu QPR sample was annealed under high vacuum to induce the formation of Nb_3Sn at the Nb/bronze interface, driven primarily by the inward diffusion of Sn from the bronze into the Nb layer [32], while minimizing undesired Sn penetration through the Nb diffusion barrier. The heat treatment involved a slow ramping process, in which the QPR sample was heated to 700 °C at a rate of 0.5 °C min^{-1} and held for 30 h. Owing to the use of a pre-deposited bronze layer as the precursor, the conventional low-temperature alloying step (≈210 °C) and intermediate Sn diffusion step (≈400 °C) were omitted [22]. This direct high-temperature growth significantly reduced the total annealing time and overall processing cost, while enabling the formation of the Nb_3Sn phase through Cu-assisted Sn diffusion and interfacial reaction with Nb. After annealing, the QPR sample was cooled to room temperature by natural cooling.

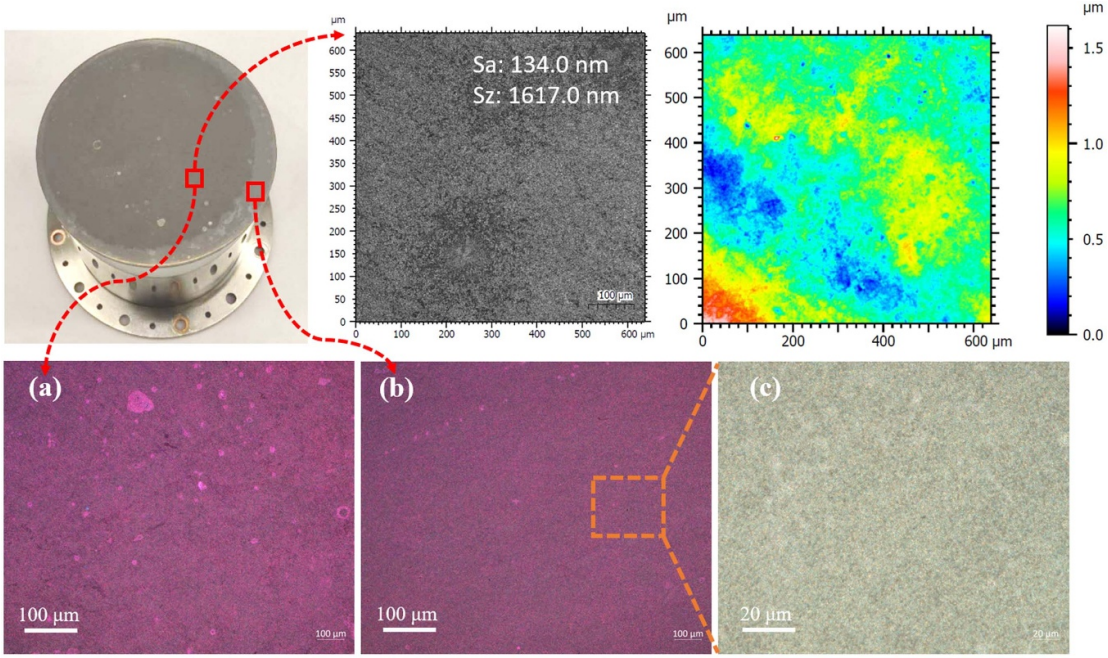

Figure 9. LSM image of the Nb_3Sn surface after surface etching, showing the surface morphology of different regions. (a) High-resolution DIC image of the high magnetic field region beneath the QPR poles. (b) High-resolution DIC image of the lighter edge region. (c) Magnified view of a small portion of the edge region shown in (b).

2.6. Nb_3Sn surface etching

Post-annealing surface etching is crucial for removing residual bronze, surface contaminants, and reaction byproducts, thereby exposing the surface Nb_3Sn layer suitable for subsequent RF characterization. A series of chemical formulations—including phosphoric acid, nitric acid, and hydrogen peroxide—were systematically evaluated for surface cleaning, among which freshly prepared aqua regia (a 3:1 volumetric mixture of 37 wt% HCl and 68 wt% HNO_3) demonstrated superior performance. This optimized formulation effectively removes surface impurities without attacking or degrading the Nb_3Sn film.

After chemical etching at 25 °C for 20 min, the samples were examined using LSM to characterize the surface roughness and morphology of the Nb_3Sn layer. As shown in figure 9, the surface exhibits noticeable voids and irregular features caused by pits on the underlying Cu substrate introduced during the electrochemical polishing process. The arithmetic Sa was measured to be 134.0 nm over an area of 600 μm × 600 μm. A comparison between the same area before and after etching could further clarify the correlation between surface voids and the underlying pits introduced during Cu electrochemical polishing. Such surface defects, especially the pits, may locally degrade RF performance.

Figures 9(a)–(c) present high-resolution differential interference contrast (DIC) images that reveal morphological and optical-contrast variations across the surface. The darker central region corresponds to near-stoichiometric Nb_3Sn, whereas the brighter corner areas indicate Sn-rich regions. This assignment is based on the estimated local current density during bronze electroplating: the edges experience higher current density, leading to a higher Sn concentration in the bronze precursor. This is attributed to higher local current density during bronze electroplating at the sample edges, resulting in increased Sn content in those regions [22]. It should be noted that the QPR primarily probes the surface resistance in the crescent-shaped region directly beneath the pole shoes of the resonator. While the edges of the sample are richer in Sn, LSM images also reveal a few tin-rich spots within this crescent-shaped region under the poles.

Following the LSM inspection, the samples were promptly transferred to a class-100 cleanroom (ISO 5) for thorough rinsing with ultrapure DI water to eliminate any residual contaminants. The rinsed samples were then dried under a flow of high-purity nitrogen gas. After drying, the samples were carefully mounted onto customized flanges compatible with the QPR system, ensuring minimal handling contamination. Finally, the assembled samples were transferred under clean conditions to the QPR test setup for RF measurements.

3. Results and discussion

To evaluate the superconducting and RF performance of the Nb_3Sn/Cu film, a comparative study was performed using both the baseline Nb/Cu sample and the ETS Nb_3Sn/Cu sample. All RF characterizations were carried out with the QPR. In parallel, microstructural and compositional analyzes were conducted on flat witness samples (30 mm × 20 mm × 3 mm) fabricated under identical processing conditions as the QPR samples.

3.1. Surface resistance and field dependence

Figure 10 compares the surface resistance R_s as a function of peak RF magnetic field measured at 413 MHz for the baseline Nb/Cu QPR sample (a) and the Cu-based Nb_3Sn QPR sample (b). At 4.5 K and 15 mT, the Nb/Cu reference exhibits a surface resistance of approximately 90 nΩ, which is higher than the values reported for state-of-the-art Nb/Cu films [33], but consistent with early-generation sputtered Nb/Cu coatings, representing medium-grade RF quality [28]. Under the same conditions, the Cu-based Nb_3Sn sample reaches a significantly lower surface resistance of 47.5 nΩ, comparable to early QPR results of vapor-diffused Nb_3Sn coatings on Nb substrates [34]. The obtained R_s value is comparable, in terms of low-field surface resistance, to early QPR results of vapor-diffused Nb_3Sn coatings on Nb substrates [34]. However, at 2 K the surface resistance is dominated by residual losses, and its slightly higher value likely reflects extrinsic factors such as trapped magnetic flux, weakly superconducting grain boundaries, or localized normal-conducting regions. Similar low-temperature behavior has also been reported for Nb_3Sn cavities fabricated by vapor diffusion, where enhanced residual resistance and field-dependent losses were mainly attributed to surface defects (e.g. Sn droplets) and flux trapping [35, 36]. These results suggest that while the bronze route Nb_3Sn/Cu coating shows promise, further optimization of the fabrication process is necessary to achieve consistently superior performance across the full operating temperature range.

The field dependence of the surface resistance $R_s(B)$ was described using different empirical models for the two types of samples: a linear approximation for the Nb/Cu reference sample and a quadratic model for the Nb_3Sn/Cu samples, in order to capture their respective field-dependent trends. To evaluate the performance difference between the Nb/Cu and Nb_3Sn/Cu samples, however, the Q-slope behavior is assessed based on the measured $R_s(B)$ at 4 K and a model-independent field-induced loss ratio, defined as $R_s(35\,\mathrm{mT})/R_s(10\,\mathrm{mT})$. As shown in figure 11(a), at 4.0 K and 413 MHz, R_s of Nb_3Sn/Cu exhibits a more significant increase with the rise of peak field B (from 10 mT to 35 mT) compared to Nb/Cu, indicating a stronger field dependence of R_s for Nb_3Sn/Cu. For the loss ratio $R_s(35\ \mathrm{mT})/R_s(10\ \mathrm{mT})$ (figure 11(b)), Nb_3Sn/Cu exhibits a higher ratio over the measured temperature range above 3 K. At 2 K, however, the ratio for Nb/Cu is comparable to or slightly higher than that of Nb_3Sn/Cu. In addition, Nb/Cu shows a relatively stable ratio at temperatures above 3 K, with a slight decreasing trend. These results suggest that Nb/Cu has better resistance to field-induced RF losses under the tested conditions, whereas Nb_3Sn/Cu shows more prominent field-dependent degradation in RF surface resistance at temperatures above 3 K.

Figure 12 shows the temperature dependence of R_s at 413 MHz for the baseline Nb/Cu QPR sample (a) and the Cu-based Nb_3Sn QPR sample (b). The measured $R_s(T)$ curves under different RF field levels were fitted using a simplified BCS-based model for both samples, expressed as:

$$R_s(T) = R_{res} + A \cdot \frac{\omega^2}{T} \exp\left(-\frac{\Delta}{k_B T}\right), \tag{1}$$

where R_{res} is the residual resistance, A is a fitting parameter related to BCS scattering, Δ is the superconducting energy gap, ω is the angular frequency of the RF field, and k_B is the Boltzmann constant. The fitting of the measured $R_s(T)$ curves under different RF field levels allowed extraction of R_{res}, A, and Δ. The extracted fitting parameters are summarized in figure 13. Compared to the Nb/Cu reference, the Nb_3Sn coating exhibits a lower residual resistance and a larger superconducting energy gap. The $R_s(T)$ fits for Nb_3Sn, however, are affected by significant uncertainties. These arise from a combination of factors, including the limited temperature range near T_c, the assumptions inherent in the implified BCS-based model, and intrinsic characteristics of the thin films such as local inhomogeneities, defects, impurities or contaminants, and residual stress [37, 38]. These effects influence key superconducting parameters, including T_c, the energy gap Δ, and the penetration depth $\lambda(T)$, and collectively contribute to the observed instability in the fitted parameters.

Figure 14 (a) presents the field dependence of R_s at 413 and 845 MHz, measured at several fixed temperatures, showing a similar trend of increasing R_s with applied RF field. At 845 MHz and 4.0 K, the surface resistance R_s of the Cu-based Nb_3Sn sample increased to 105 nΩ at 15 mT. Figure 14(b) shows the

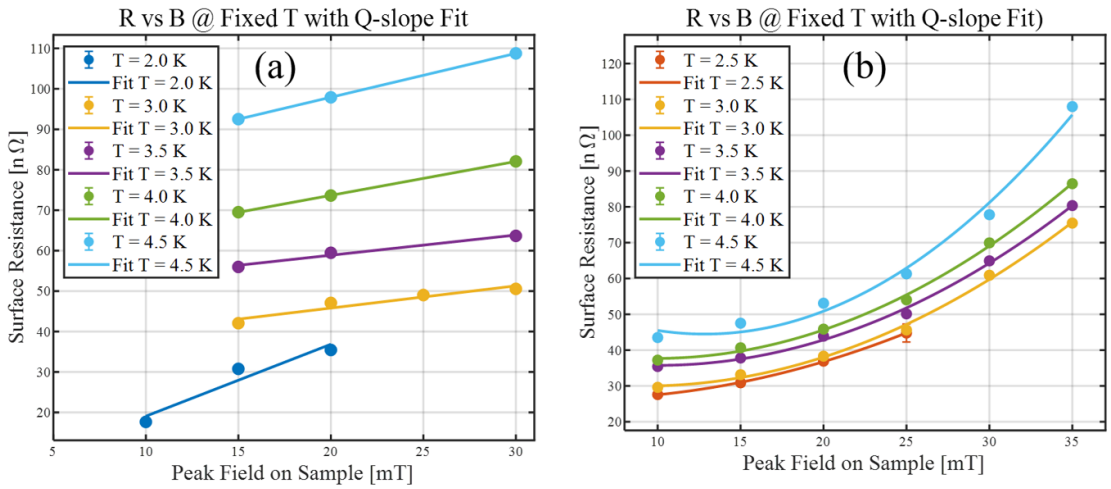

Figure 10. Surface resistance R_s as a function of peak RF magnetic field measured at 413 MHz: (a) baseline Nb/Cu QPR sample; (b) Cu-based Nb_3Sn QPR sample.

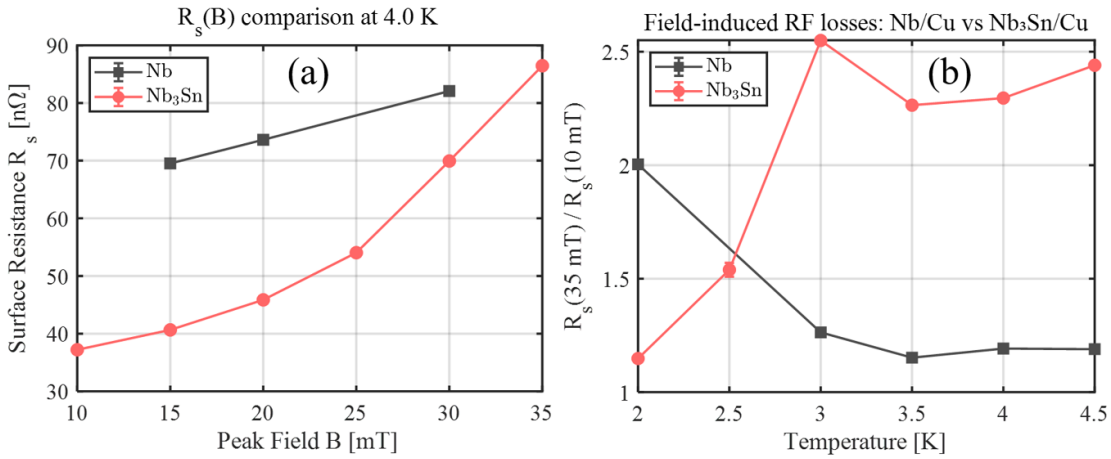

Figure 11. Field dependence of the RF surface resistance at 413 MHz: (a) comparison of $R_s(B)$ for Nb/Cu and Nb_3Sn/Cu at 4.0 K; (b) field-induced RF losses for Nb/Cu and Nb_3Sn/Cu expressed as $R_s(35\,\mathrm{mT})/R_s(10\,\mathrm{mT})$.

peak-field dependence of the R_{res} and R_{BCS} at 413 and 845 MHz. R_{res} exhibits a weak increase with field, while R_{BCS} remains relatively small at low temperatures.

3.2. Superconducting transition and quench behavior

The temperature dependence of the RF penetration depth $\lambda(T)$, shown in figure 15, was obtained from the measured frequency shift $f(T)$ in the QPR and subsequently calibrated using a reference Nb sample with a known $\lambda(T)$. For the Nb/Cu reference sample (a), the superconducting transition is centered around 9.2 K, slightly lower than the typical T_c of bulk Nb, which can be attributed to oxygen incorporation in sputtered Nb films [39]. For the Cu-based Nb_3Sn sample (b), the $\lambda(T)$ fit for the Cu-based Nb_3Sn sample was restricted to data above 11 K to ensure reliable fitting. The transition occurs at $T_c \approx 14.6$ K and appears broader. This may be partly due to the fitting procedure, but is also consistent with the intrinsic behavior of Nb_3Sn, whose T_c varies with local Sn content, such that regions with slightly lower Sn exhibit reduced T_c. Additional factors such as internal strain, microstructural defects, and composition inhomogeneity may also contribute to the observed transition width and could slightly reduce T_c [16].

Figure 16 compares the temperature dependence of the RF quench field for the two samples. For the Nb/Cu reference, a T^2 fit to the data in the 8–9 K range yields an extrapolated zero-temperature quench field of approximately 257 mT, close to the theoretical superheating field of niobium. For the Cu-based Nb_3Sn sample, the extrapolated quench field is approximately 56.3 mT at 0 K. Although this value is significantly lower than the theoretical superheating field of Nb_3Sn (>400 mT), it remains above the

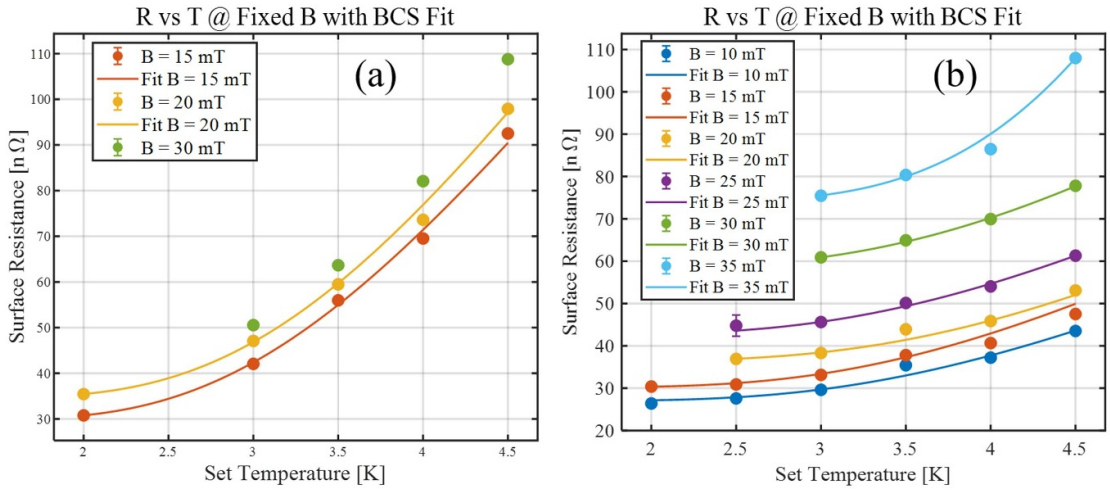

Figure 12. Temperature dependence of the RF surface resistance R_s measured at 413 MHz: (a) baseline Nb/Cu QPR sample; (b) Cu-based Nb_3Sn QPR sample.

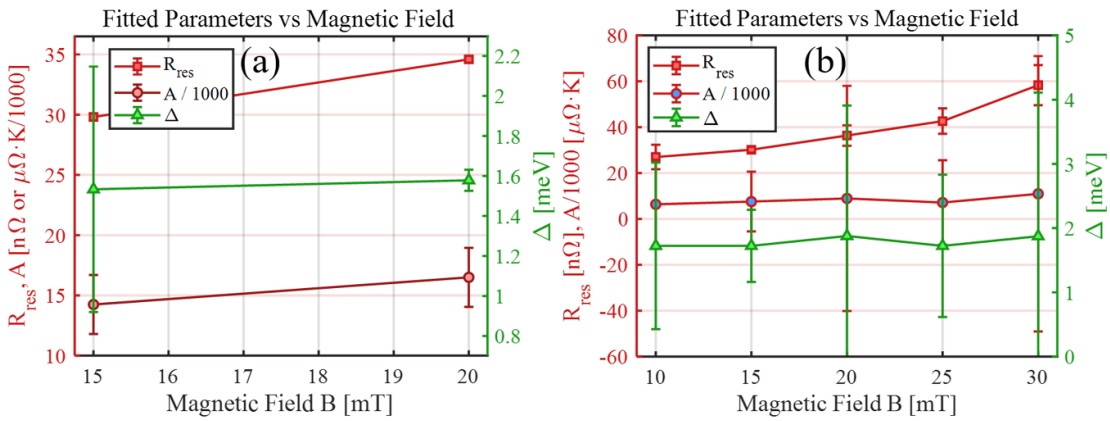

Figure 13. Extracted BCS fitting parameters as a function of peak RF magnetic field: (a) baseline Nb/Cu QPR sample; (b) Cu-based Nb_3Sn QPR sample.

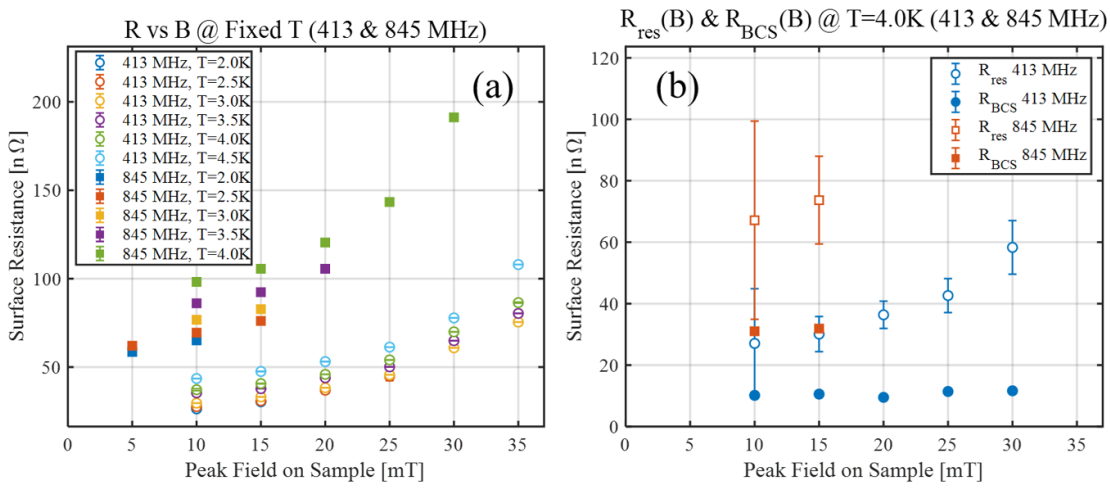

Figure 14. (a) Field dependence of the R_s of the Cu-based Nb_3Sn sample at 413 and 845 MHz, measured at several fixed temperatures. (b) R_{res} and R_{BCS} vs. peak RF field at 413 MHz (blue) and 845 MHz (orange) at $T = 4.0$ K.

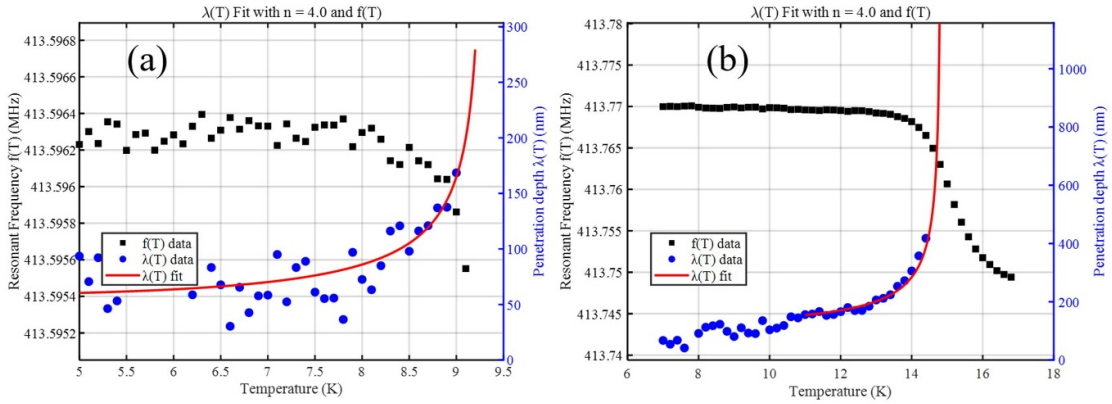

Figure 15. Temperature dependence of the RF penetration depth $\lambda(T)$: (a) baseline Nb/Cu QPR sample; (b) Cu-based Nb_3Sn QPR sample..

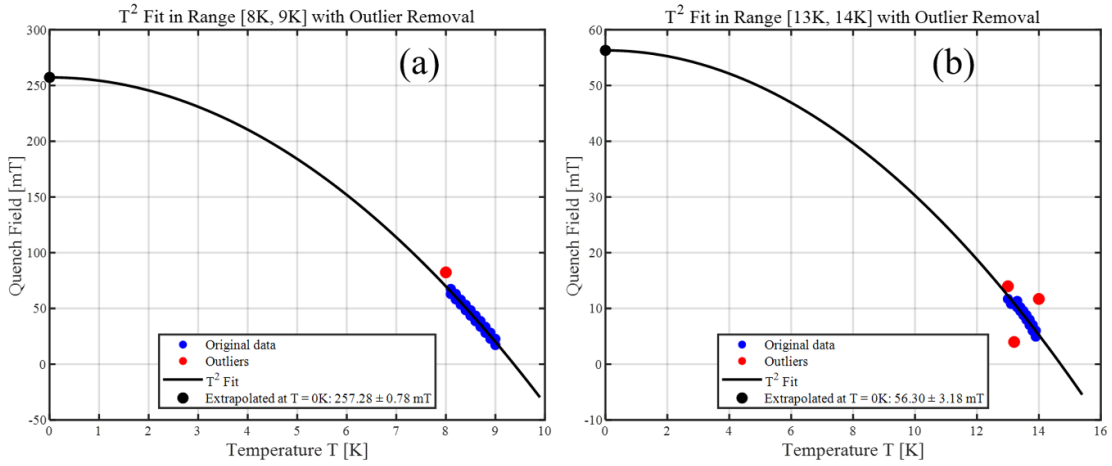

Figure 16. Temperature dependence of the RF quench field: (a) baseline Nb/Cu QPR sample; (b) Cu-based Nb_3Sn QPR sample.

Table 3. Material parameters derived from surface resistance $R_s(T)$, penetration depth, and quench field for Nb/Cu and Nb_3Sn/Cu QPR samples measured at 412–413 MHz and 15–20 mT, together with reference values for ECR Nb/Cu and tin vapor diffusion Nb_3Sn QPR samples [41, 42].

Symbol	Nb/Cu	Nb_3Sn/Cu	ECR Nb/Cu Aull2023jwy	Nb_3Sn/Nb [42]
$\lambda(0)$ [nm]	58.0 ± 6.0	123.6 ± 5.4	37 ± 2	159.0 ± 2.0
ℓ [nm]	16.8 ± 6.4	5.0 ± 0.8	182 ± 24	2.4 ± 0.1
RRR	6.2 ± 2.4	4.2 ± 0.7	67 ± 9	2.0 ± 0.1
T_c [K]	9.20 ± 0.19	14.71 ± 0.06	9.36 ± 0.01	18.91 ± 0.01
R_{res} [nΩ]	34.6 ± 0.3	30.2 ± 1.3	29.6 ± 0.6	≈ 43
A_{BCS} [$\mu\Omega \cdot$ K]	16.5 ± 2.5	7.6 ± 1.3	10.01 ± 1.6	≈ 16.1
$\Delta(0)/k_B T_c$	1.58 ± 0.05	1.72 ± 0.56	2.02 ± 0.03	≈ 2.09
$B_{quench}(0)$ [mT]	257.3 ± 0.8	56.3 ± 3.2	248 ± 5	200 ± 5
$R_s(35\text{ mT})/R_s(10\text{ mT})$	1.6 (2.5 K)	2.3 (4 K)	1.3 (2.5 K)	1.6 (4 K)

Note: $\lambda(0)$ is obtained from a BCS-like fit ($n = 4$); ℓ is derived from $\lambda(0)$, and RRR from ℓ/ℓ_0.

lower critical field ($H_{c1} \approx 38$ mT) [40], suggesting that the quench is likely limited by localized thermal or structural defects rather than by vortex penetration. The reduced quench field likely reflects extrinsic factors such as Sn-rich regions, compositional inhomogeneity, or weakly connected grain boundaries, which can trigger premature vortex entry or thermal runaway under RF excitation.

Table 3 summarizes the superconducting parameters derived from surface resistance $R_s(T)$ fitting, penetration depth analysis, and quench field measurements for the Nb/Cu and Nb_3Sn/Cu QPR samples, together with reference values for ECR Nb/Cu and tin vapor diffusion Nb_3Sn/Nb samples reported in the literature [41, 42]. It should be noted that, in this table, the $\lambda(T)$ fitting is performed over a limited

Table 4. Comparison of representative QPR-measured surface resistance (R_s) and quench field values of Nb_3Sn coatings at 4.5 K and ∼15 mT (400–417 MHz). Data are extracted from this work and published references.

Method	Substrate	Freq. (MHz)	R_s (nΩ)	B_q (mT)
Bronze route (this work)	Cu	413	47.5	56.3
HiPIMS + annealing [43]	Cu	∼400	50–60	—
DCMS [43]	Cu	∼400	>100	—
Sn vapor diffusion [44]	Nb	414	∼50	200±5
Sputtering [45]	Nb	417	∼20	>70

number of temperature points, which naturally leads to larger statistical uncertainties in the extracted zero-temperature penetration depth $\lambda(0)$. This increased uncertainty further propagates into the estimation of the electron mean free path ℓ and, consequently, into the derived residual resistivity ratio (RRR) values. Compared to the reference samples, the Nb_3Sn/Cu sample exhibits a substantially larger penetration depth $\lambda(0)$, a much shorter mean free path ℓ, an extremely low RRR, a reduced critical temperature T_c, and a lower quench field B_{quench}, all of which indicate enhanced electronic scattering and increased disorder, likely arising from the Cu-related inclusions and microstructural imperfections. These observations highlight the challenges of achieving high-quality Nb_3Sn coatings on copper and the need for improved control over composition and microstructure for SRF applications.

To contextualize the RF performance of the present Cu-based Nb_3Sn coatings, table 4 summarizes representative R_s values at 4.5 K and ∼15 mT obtained from different Nb_3Sn coating methods on both Cu and Nb substrates. These values were extracted from figures and data reported in recent literature [34, 44]. The table provides a comparative view of performance across diverse deposition techniques, including HiPIMS, DCMS, Sn-vapor diffusion, and optimized sputtering, highlighting both typical R_s and quench behavior. Among the tested techniques, the bronze route currently exhibits the lowest surface resistance on Cu substrates, demonstrating its potential as a promising pathway for SRF applications operating at 4.5 K.

3.3. Surface morphology and compositional analysis of the Cu-based Nb_3Sn small sample

To assess the microstructural quality and phase composition of the Cu-based Nb_3Sn coating, scanning electron microscopy (SEM), EDX, and x-ray diffraction (XRD) were performed on a small witness sample prepared under identical conditions.

As shown in figure 17(a), the SEM image reveals a continuous Nb_3Sn coating consisting of grains ranging in size from 100 nm to 600 nm. The grains appear well-connected, and no extended cracks or voids were detected. Nevertheless, the presence of surface impurity particulates and a broad Nb_3Sn grain size distribution suggests local inhomogeneity, which may contribute to nonuniform RF losses. The XRD pattern in figure 17(b), measured in Bragg–Brentano geometry, confirms that the dominant phase is the A15 Nb_3Sn structure, with strong reflections such as (200), (210), and (211), consistent with polycrystalline A15 growth. The average crystallite size estimated from the (200) peak broadening is ∼47 nm similar to magnteron-sputtered films [12]. The smaller crystallite size estimated from XRD reflects coherently scattering domains rather than entire grains observed in SEM. In addition to the dominant A15 reflections, several weak peaks are observed. Some of these weaker signals likely originate from the Nb diffusion barrier layer and the Cu substrate as the effective x-ray probing depth of Nb_3Sn governed by x-ray absorption is relatively high, and varies between 2.2–5.7 μm for x-ray incidence angles $\Theta = 20 - 60°$, respectively [46]. Minor peaks near the expected $NbSn_2$ positions may indicate residual secondary phases or local deviations in stoichiometry, but they do not dominate the overall phase composition.

The EDX measurements were performed using electron beam energies E_0 = 5 keV and 10 keV. The corresponding analytical depths were estimated using a Castaing-type semi-empirical approximation, in which the analytical depth scales with material parameters and beam energy as

$$z_{EDX} \propto \frac{A}{\rho Z}\left(E_0^{1.7} - E_c^{1.7}\right), \tag{2}$$

assuming continuous energy loss and homogeneous material properties [47]. Here A is the atomic weight (amu), ρ is the density (g cm^{-3}), Z is the atomic number, E_0 is the beam energy (keV), and E_c is the critical excitation energy (keV). Using this approach, analytical depths of 0.02 μm (0.07 μm) and 0.31 μm (0.36 μm) were obtained for pure Nb (Sn), respectively. In contrast, the maximal penetration depth of primary electrons was estimated using the Kanaya–Okayama expression [48], yielding R = 0.16 μm (5 keV) and R = 0.50 μm (10 keV) for Nb_3Sn (density 8.9 g cm^3). As the x-ray generation

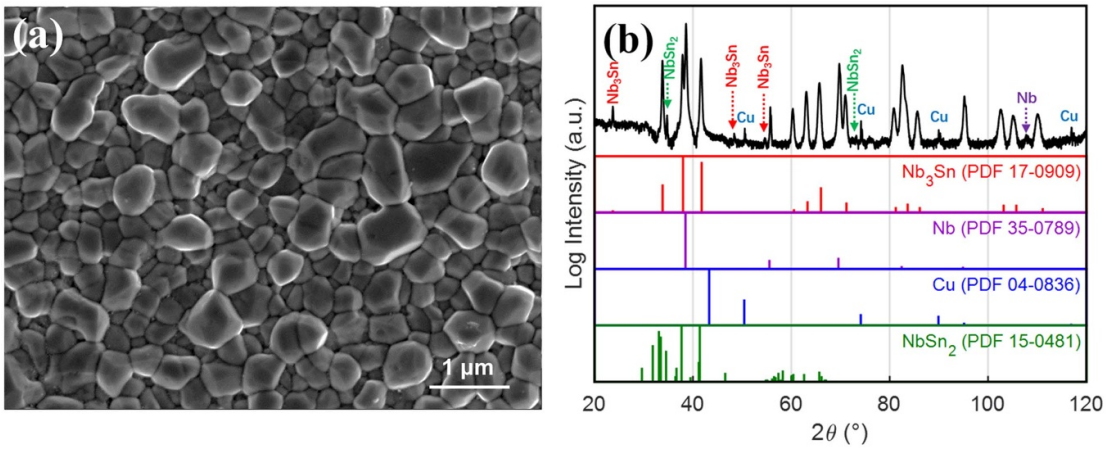

Figure 17. Surface characterization of the Cu-based Nb_3Sn sample. (a) SEM image showing a granular Nb_3Sn surface with moderately fine grains and surface particulates. (b) XRD pattern indicating dominant A15 Nb_3Sn phase along with weak contributions from secondary Nb–Sn intermetallics.

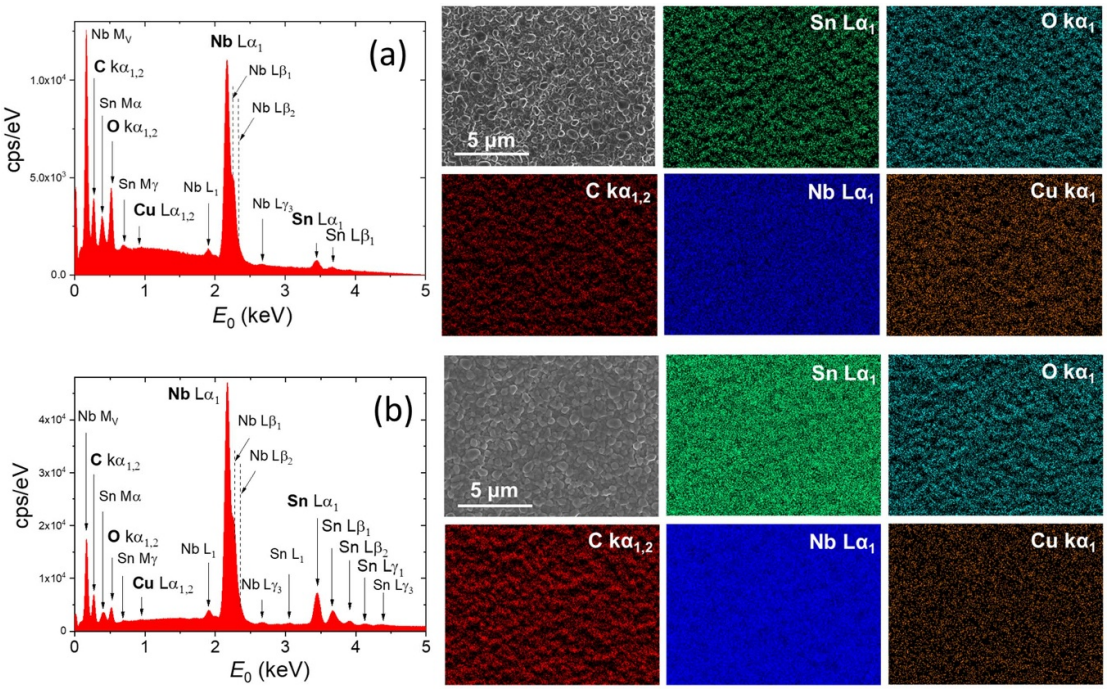

Figure 18. The EDX spectra and the corresponding elemental maps obtained at $E_0 = 5$ keV (a) and $E_0 = 10$ keV (b) of the Cu-based Nb_3Sn sample. The energy corresponding to Cu $L\alpha_1$ peak is pointed out with an arrow.

distribution is non-uniform and x-ray absorption further limits the detectable signal, the effective EDX information depth is typically a fraction of the electron penetration depth, approximately $(0.2-0.6)\cdot R$.

The average Nb/Sn ratios calculated from the spectra acquired at five different sample locations are 2.99 (5 keV) and 3.84 (10 keV). Thus, the Sn content determined at 5 keV corresponds to the stoichiometric 25 at.% within the accuracy of EDX measurements. The higher niobium content obtained at $E_0 = 10$ keV is evidently due to contribution from the underlying niobium buffer layer. No copper particles or copper-enriched regions were observed at the sample surface. Trace amounts of copper (0.1%–0.9 at.%) were detected only at $E_0 = 10$ keV which is attributed to the substrate as the areas with smaller (around 100 nm) Nb_3Sn grain dimensions are present at the surface, likely due to micro-scale surface pits exposing the underlying Cu.

Figure 18 shows the EDX spectra and the corresponding elemental maps obtained at $E_0 = 5$ keV and $E_0 = 10$ keV. The resulting atomic composition has the following values: Nb 47.6 at.%(33.7 at.%), Sn 16.1 at.%(8.7 at.%), O 10.4 at.%(7.4 at.%), Cu 0 at.%(0.1 at.%), and C 25.9 at.%(50.1 at.%) for $E_0 =$ 5 keV(10 keV), correspondingly. An apparent high carbon content is consistent with known artefacts of

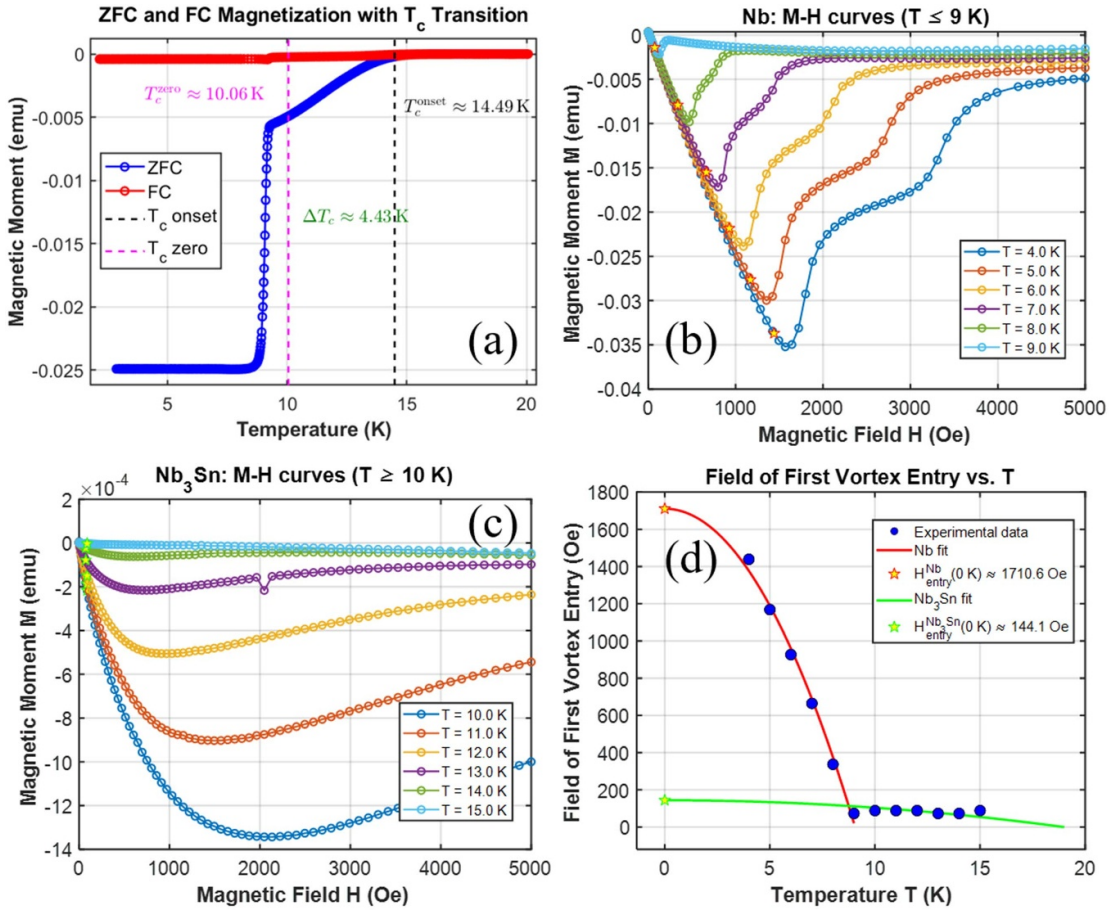

Figure 19. Magnetization and lower critical field measurements of the Cu-based Nb_3Sn sample. (a) ZFC/FC magnetization curves showing the superconducting transitions of the Nb barrier and Nb_3Sn layer. (b) Nb barrier layer: M–H curves ($T \leqslant 9$ (K). (c) Nb_3Sn layer: M–H curves ($T \geqslant 10$ (K). (d) Temperature dependence of the field of first vortex entry with empirical fitting results.

EDX, as the technique commonly overestimates surface carbon due to adventitious hydrocarbon contamination. Elemental mapping indicates that Nb and Sn are relatively uniformly distributed across the surface of this flat test sample, suggesting the formation of a continuous Nb_3Sn layer. While local variations may exist on the actual QPR sample due to its curved geometry and surface features, the mapping provides a representative illustration of the general film formation process. The relatively high O and C fractions point to contamination, likely from surface oxidation and adsorbates, which are known to increase RF surface resistance in SRF applications. The fact that XRD analysis did not reveal any oxides suggests that either their quantity is below the detection limit or they are in an amorphous state.

The superconducting properties of the Cu-based Nb_3Sn sample were further investigated using a physical property measurement system (PPMS), as shown in figure 19. In figure 19(a), the zero-field-cooled (ZFC) and field-cooled (FC) magnetization curves reveal a superconducting transition with an onset temperature of $T_c^{onset} \approx 14.49$ K and a zero-resistance temperature of $T_c^{zero} \approx 10.06$ K, corresponding to a transition width of $\Delta T_c \approx 4.43$ K. The relatively broad transition suggests compositional and structural inhomogeneity, consistent with the SEM and XRD results. Figures 19(b) and (c) show the magnetization–field (M–H) curves measured for the Nb barrier layer ($T \leqslant 9$ K) and the Nb_3Sn layer ($T \geqslant 10$ K), respectively. The magnetic field was applied parallel to the film surface, and the field of first vortex entry, $H_{entry}(T)$, was quantitatively determined for each temperature by analyzing the local slope of the M–H curve using a sliding-window linear fit; the field at which the slope exhibits the maximum deviation from the initial linear Meissner response was identified as the first vortex entry field. The temperature dependence of the first vortex-entry field $H_{entry}(T)$ for both layers is summarized in figure 19(d). Fitting the data using the empirical relation $H_{entry}(T) = H_{entry}(0)\left[1-(T/T_c)^2\right]$ yields $H_{entry}^{Nb}(0) \approx 1710.6$ Oe (fit below 9 K) for the Nb barrier layer and $H_{entry}^{Nb_3Sn}(0) \approx 144.1$ Oe (fit above 10 K) for the Nb_3Sn coating. Measured under near-ideal conditions, the extracted H_{entry} is expected to closely approximate the intrinsic H_{c1} if the superconducting thin-film quality is sufficiently high, thereby providing a qualitative yet meaningful reference for assessing the film performance. While the Nb film

exhibits values consistent with bulk Nb, the reduced $H_{entry}(0)$ observed for Nb_3Sn likely reflects limited phase purity and possible weak-link effects at grain boundaries.

From the perspective of SRF applications, these results demonstrate the successful formation of a superconducting Nb_3Sn layer on the Cu substrate. However, further optimization is required to improve stoichiometry, reduce surface tin-rich performance-degrading phases, mitigate oxygen contamination, increase Nb_3Sn film density, and relieve its internal stress. Enlarging the grain size to minimize flux pinning and sharpening the superconducting transition are also essential. Such improvements are expected to raise the effective T_c above 17 K and reduce the RF surface resistance, thereby enhancing the Nb_3Sn/Cu system for high-performance SRF applications.

3.4. Discussion: Cu-mediated phase evolution and superconducting homogeneity in Low-Sn bronze-route Nb_3Sn coatings

The phase-formation mechanism in Cu–Sn–Nb systems fundamentally differs from the direct Nb–Sn interdiffusion model commonly observed in binary Nb–Sn coatings. In the bronze-route process, Sn primarily diffuses through the Cu-rich bronze matrix rather than directly through Nb. During annealing, Sn initially reacts with Cu to form Cu–Sn intermetallic layers such as η–Cu_6Sn_5 and ε–Cu_3Sn [16]. As annealing progresses, Sn is gradually released from these intermediates and migrates along Cu grain boundaries and the Cu/Nb interface, where it reacts with Nb to form the A15 Nb_3Sn phase [18, 19]. This Cu-assisted reaction pathway explains the absence of direct Nb–Sn interdiffusion and accounts for the persistence of Cu-rich inclusions and Sn-rich residual phases in the coating. Such Cu-related and Sn-rich phases (e.g. η, ε, $NbSn_2$, Nb_6Sn_5) are generally tolerable in DC multifilamentary wires, where they have a minor impact on transport J_c. In RF applications, however, they act as normal-conducting inclusions, increasing surface dissipation and promoting premature quenching [2].

In this experiment, the bronze precursor was electroplated with a relatively low Sn content (10 at.%). Under such conditions, the formation of bulk η and ε phases is thermodynamically unlikely during both plating and subsequent annealing [32]. Nevertheless, EDX and XRD analyzes detected trace amounts of these secondary phases together with localized Cu enrichment near the Nb_3Sn/Cu interface, in agreement with previous reports on bronze-route coatings [14, 49, 50]. These findings support a Cu-mediated growth mechanism and emphasize the importance of optimizing diffusion barriers and post-annealing etching to suppress detrimental phases and improve RF homogeneity. Furthermore, precise control of the Sn supply, annealing conditions, and diffusion-barrier integrity is essential for promoting complete A15 formation and minimizing performance-degrading phases.

Although the measured transition temperature ($T_c \approx 14.6$ K) is lower than the stoichiometric value of Nb_3Sn (18 K), such a reduction is common in Cu-based Nb_3Sn coatings. EDX indicates that the film is Sn-deficient on average—consistent with an Sn content below the 25 at.% required for stoichiometric A15—while XRD and SEM reveal minor Nb–Sn secondary phases and local compositional inhomogeneity. These results indicate incomplete and non-uniform A15 formation across the coating. In addition, oxygen/carbon impurities, the possible presence of NbC or NbO_x, and microstructural disorder from thermal-expansion mismatch can all further depress the local T_c [49, 50]. Trace Cu detected at grain boundaries is not expected to directly alter the intrinsic T_c of A15 Nb_3Sn, but its segregation can indirectly influence the effective transition by modifying local Sn diffusion and promoting compositional gradients. Therefore, the observed 14.6 K should be interpreted as a spatially averaged effective transition temperature under the current processing conditions. These observations highlight clear processing levers for increasing the effective T_c, including increasing the Nb barrier thickness, optimizing the bronze composition and annealing profile, improving chemical etching, considering a Ta interlayer and minimizing impurity incorporation.

4. Conclusion and outlook

In this study, we have successfully demonstrated the fabrication and RF characterization of a Cu-based Nb_3Sn sample via an improved ETS bronze route, specifically tailored for QPR testing. The process integrates a series of critical advancements tailored for application on Cu substrates, including high-quality electrochemical polishing of the Cu surface, dense Nb diffusion barrier deposition via HiPIMS, uniform bronze precursor plating, controlled low-temperature annealing at 700 °C, and an optimized chemical etching procedure for surface purification. These developments effectively address key material challenges such as Cu and Nb_3Sn interdiffusion and surface Cu inclusions. The resulting Nb_3Sn coating achieved continuous coverage with clear A15 phase formation and minimal surface contamination.

RF measurements using a multi-frequency QPR revealed promising performance of the Cu-based Nb_3Sn sample. A minimum surface resistance of 47.5 nΩ was achieved at 4.5 K and 15 mT at 413 MHz,

significantly outperforming earlier Cu-based Nb_3Sn films synthesized via DCMS or HiPIMS + annealing [43]. The superconducting transition temperature was measured to be approximately 14.6 K, suggesting successful Nb_3Sn phase formation, although the relatively broad transition indicates some degree of compositional inhomogeneity, likely due to Sn deficiency or excess in certain regions. The frequency-dependent surface resistance and field-induced Q-slope observed at both 413 MHz and 845 MHz point toward extrinsic loss mechanisms, such as residual oxides and substoichiometric regions. The extrapolated intrinsic quench field of 56.3 mT, while encouraging, remains below the theoretical limit, emphasizing the need for further refinement in barrier layer design and thermal processing to suppress weak links and enhance grain boundary connectivity.

To further improve the performance of Nb_3Sn coatings on Cu substrates via the bronze route, future efforts will focus primarily on optimizing the diffusion barrier design. This includes increasing the Nb barrier layer thickness to 30 μm or more and enhancing its density to more effectively suppress Cu diffusion during annealing. The incorporation of an additional Ta diffusion barrier is also being considered. Concurrently, further refinement of the thermal treatment profile will be pursued to promote phase purity and uniform Sn distribution throughout the coating. Development of tailored chemical etching and surface cleaning protocols for the Nb_3Sn film will also be essential to reduce contamination and eliminate surface-related defects. These improvements aim to enable reliable, scalable fabrication of high-performance Nb_3Sn/Cu structures for SRF applications. The bronze route may not yet rival vapor-diffused Nb_3Sn in ultimate performance, but it offers a low-temperature, Cu-compatible route with clear room for process optimization. In the near term, achievable RF performance will likely remain below that of optimized Nb_3Sn on Nb substrates, but continued improvements in diffusion-barrier engineering and Sn-uniformity control may gradually close this gap.

Overall, this work provides compelling evidence for the feasibility of the bronze route in producing high-quality Nb_3Sn coatings directly on Cu substrates at temperatures compatible with large-scale SRF cavity production. Compared to traditional Nb/Cu multilayers and bulk Nb structures, the Nb_3Sn/Cu combination offers improved performance at elevated temperatures (e.g. 4.2–4.5 K), reduced cryogenic load, and greater cost-efficiency. The current results represent an important milestone toward realizing fully functional Nb_3Sn/Cu SRF cavities. Future efforts will focus on eliminating residual impurities, optimizing phase stoichiometry, and scaling the process to elliptical cavities operating at 1.3 GHz. With continued process development, the bronze route holds strong potential for enabling the next generation of high-performance, energy-efficient Nb_3Sn SRF accelerators.

Taken together, these results provide concrete advances within the long-standing bronze-route research path. By delivering the first quantitative QPR benchmark of a bronze-route Nb_3Sn coating on a Nb/Cu substrate, this work establishes a reference point for evaluating the realistic RF capabilities of this materials system. The combined microscopy, magnetometry and penetration–depth analysis further clarifies which microstructural features most critically limit T_c, quench field and residual resistance in the present coatings. Finally, the demonstrated ETS-based preparation route is compatible with conduction-cooled SRF concepts, thereby offering a realistic platform for future optimization of Cu-based Nb_3Sn technologies.

Acknowledgments

We gratefully acknowledge I Rudolph for technical support in the chemical facilities at the WI-APG department of HZB. We also thank R Feyerherm from the QM-IQM department at HZB for performing the PPMS measurements. This work has received partial funding from the European Union's Horizon 2020 Research and Innovation programme under Grant Agreement No. 101004730 (I.FAST). Additional support was provided by the German Federal Ministry of Education and Research (BMBF) under Grant No. 100636506 (CavitySusOp, within the SuperSurfer framework).

Data availability statement

All data that support the findings of this study are included within the article (and any supplementary files).

Author contributions

Ming Lu 0009-0003-4817-5053
Conceptualization (equal), Data curation (equal), Formal analysis (equal), Investigation (equal), Methodology (equal), Software (equal), Validation (equal), Visualization (equal), Writing – original draft (equal), Writing – review & editing (equal)

Sebastian Keckert 0000-0003-2235-5315
Data curation (equal), Resources (equal), Software (equal), Validation (equal), Writing – review & editing (equal)

Felix Kramer
Investigation (equal), Methodology (equal), Resources (equal), Software (equal)

Alena Prudnikava 0000-0003-0647-2546
Investigation (equal), Resources (equal), Software (equal), Writing – review & editing (equal)

Jens Knobloch 0000-0003-1382-3826
Funding acquisition (equal), Project administration (equal), Resources (equal), Supervision (equal), Writing – review & editing (equal)

Aleksandr Zubtsovskii
Investigation (equal), Methodology (equal), Resources (equal), Visualization (equal)

Oliver Kugeler 0000-0003-0157-2118
Funding acquisition (equal), Methodology (equal), Project administration (equal), Resources (equal), Supervision (equal), Writing – review & editing (equal)

References

[1] Posen S, Liepe M and Hall D L 2015 Proof-of-principle demonstration of Nb_3Sn superconducting radiofrequency cavities for high Q_0 applications *Appl. Phys. Lett.* **106** 082601
[2] Posen S and Hall D L 2017 Nb_3Sn superconducting radiofrequency cavities: fabrication, results, properties and prospects *Supercond. Sci. Technol.* **30** 033004
[3] Jiang G *et al* 2024 Understanding and optimization of the coating process of the radio-frequency Nb_3Sn thin film superconducting cavities using tin vapor diffusion method *Appl. Surf. Sci.* **643** 158708
[4] Posen S, Lee J, Seidman D N, Romanenko A, Tennis B, Melnychuk O S and Sergatskov D A 2021 Advances in Nb_3Sn superconducting radiofrequency cavities towards first practical accelerator applications *Supercond. Sci. Technol.* **34** 025007
[5] Sun Z, Baraissov Z, Porter R D, Shpani L, Shao Y-T, Oseroff T, Thompson M O, Muller D A and Liepe M U 2023 Smooth, homogeneous, high-purity Nb_3Sn superconducting RF resonant cavity by seed-free electrochemical synthesis *Supercond. Sci. Technol.* **36** 115003
[6] Ilyina E A, Rosaz G, Descarrega J B, Vollenberg W, Lunt A J G, Leaux F, Calatroni S, Venturini-Delsolaro W and Taborelli M 2019 Development of sputtered Nb_3Sn films on copper substrates for superconducting radiofrequency applications *Supercond. Sci. Technol.* **32** 035002
[7] Stilin N A, Holic A, Liepe M, Porter R D, Sears J and Sun Z 2023 RF and thermal studies on conduction cooled Nb_3Sn SRF cavity *Eng. Res. Express* **5** 025078
[8] Ciovati G, Cheng G, Pudasaini U and Rimmer R A 2020 Multi-metallic conduction cooled superconducting radio-frequency cavity with high thermal stability *Supercond. Sci. Technol.* **33** 07LT01
[9] Barzi E *et al* 2022 An impartial perspective for superconducting Nb_3Sn coated copper RF cavities for future accelerators (arXiv:2203.09718)
[10] Barzi E and Mattafirri S 2002 Kinetics of phase growth in Nb_3Sn formation for heat treatment optimization *FERMILAB Conf. Report* (*Batavia, IL, USA, 2002*) *FERMILAB Conf. Report* (Fermi National Accelerator Laboratory)
[11] Ciovati G *et al* 2023 Development of a prototype superconducting radio-frequency cavity for conduction-cooled accelerators *Phys. Rev. Accel. Beams* **26** 044701
[12] Sayeed M N, Pudasaini U, Reece C E, Eremeev G V and Elsayed-Ali H E 2021 Properties of Nb_3Sn films fabricated by magnetron sputtering from a single target *Appl. Surf. Sci.* **541** 148528
[13] Carta G, Rossetto G Zanella P, Crociani L, Palmieri V and Todescato F 2006 Attempts to deposit Nb_3Sn by MOCVD *9th Int. Workshop on Thin Films for RF Superconductivity* (JACoW Publishing)
[14] Withanage W K, Juliao A and Cooley L D 2021 Rapid Nb_3Sn film growth by sputtering Nb on hot bronze *Supercond. Sci. Technol.* **34** 06LT01
[15] Rey C M, Eremeev G and Valente-Feliciano A-M 2021 Investigations towards ultra-low cost Nb_3Sn SRF cavity fabrication via melt casted bronze route processing *IEEE Trans. Appl. Supercond.* **31** 1–4
[16] Godeke A 2006 A review of the properties of Nb_3Sn and their variation with A15 composition, morphology and strain state *Supercond. Sci. Technol.* **19** R68
[17] Laurila T, Vuorinen V, Kumar A.K and Paul A 2010 Diffusion and growth mechanism of Nb_3Sn superconductor grown by bronze technique *Appl. Phys. Lett.* **96** 231910
[18] Barzi E, Bestetti M, Reginato F, Turrioni D and Franz S 2015 Synthesis of superconducting Nb_3Sn coatings on Nb substrates *Supercond. Sci. Technol.* **29** 015009

[19] Ito H, Hayano H, Monjushiro H, Kashiwagi S, Honda F, Kikuchi A and Barzi E 2020 Nb_3Sn formation using electroplating method for SRF cavity *Proc. 17th Annual Meeting of the Particle Accelerator Society of Japan (PASJ2020)* (*Japan*) pp 193–6
[20] Sandim M J R, Tytko D, Kostka A, Choi P, Awaji S, Watanabe K and Raabe D 2013 Grain boundary segregation in a bronze-route Nb_3Sn superconducting wire studied by atom probe tomography *Supercond. Sci. Technol.* **26** 055008
[21] Lu M *et al* 2022 Development and performance of the first Nb_3Sn thin-film cavity via bronze process *Chin. Phys. Lett.* **39** 115201
[22] Lu M, Zhang J, Luo D, Zhang B, He Y, Chu Q, Wu A, Huang S and Tan T 2025 The impact of Cu/Sn precursor tin content on the properties and growth mechanism of Nb_3Sn thin films via bronze methods *Phys. Scr.* **100** 085996
[23] Chiaveri E, Haebel E, Mahner E and Tessier J-M 1998 The quadrupole resonator: construction, RF system, field calculations and first applications *6th European Particle Accelerator Conf. (EPAC '98)* (CERN)
[24] Junginger T 2012 Investigations of the surface resistance of superconducting materials *PhD Thesis* Ruprecht–Karls–Universität Heidelberg (https://doi.org/10.11588/heidok.00013728)
[25] Kleindienst R 2017 Radio frequency characterization of superconductors for particle accelerators *PhD Thesis* Universität Siegen
[26] Keckert S 2019 Characterization of Nb_3Sn and multilayer thin films for SRF applications *PhD Thesis* Universität Siegen (https://doi.org/10.25819/ubsi/1487)
[27] Keckert S, Kleindienst R, Kugeler O, Tikhonov D and Knobloch J 2021 Characterizing materials for superconducting radiofrequency applications—a comprehensive overview of the quadrupole resonator design and measurement capabilities *Rev. Sci. Instrum.* **92** 064710
[28] Keckert S *et al* 2021 Mitigation of parasitic losses in the quadrupole resonator enabling direct measurements of low residual resistances of SRF samples *AIP Adv.* **11** 125326
[29] Sil'chenko D, Reznichenko G, Maksimenko O, Pancheva H, Mykhailova E and Pylypenko O 2022 Studying the effect of butanol on the anode behavior of copper in phosphoric acid solutions *Chem. Chem. Technol.* **16** 103–11
[30] Leith S *et al* 2023 HiPIMS deposition of superconducting Nb thin films onto Cu substrates *Vacuum* **212** 112041
[31] Lu M, Pan F, Guo H, Huang S, Yang Z, Chu Q, Liu F, Wu A and Tan T 2021 Electrochemical and thermal synthesis of Nb_3Sn coatings on Nb substrates *Mater. Lett.* **292** 129557
[32] Banno N 2023 Low-temperature superconductors: Nb_3Sn, Nb_3Al and NbTi *Superconductivity* **6** 100047
[33] Arzeo M, Avino F, Pfeiffer S, Rosaz G, Taborelli M, Vega-Cid L and Venturini-Delsolaro W 2022 Enhanced radio-frequency performance of niobium films on copper substrates deposited by high power impulse magnetron sputtering *Supercond. Sci. Technol.* **35** 04
[34] Calatroni S 2021 Materials for SCRF cavities: Beyond niobium. Indico presentation at JUAS 2021, February 2021 *With Contributions From Cornell U., Fnal, Icmab* (INFN-LNL, JLAB, STFC, Temple U., Uppsala U)
[35] Chen Q, Zong Y, Wang Z, Xing S, Wu J, Dong P, Zhao M, Wu X, Rong J and Chen J 2024 First results of Nb_3Sn coated cavity by vapor diffusion method at SARI *Coatings* **14** 2024
[36] Pudasaini U, Reece C E and Tiskumara J K 2022 Managing Sn-supply to tune surface characteristics of vapor-diffusion coating of Nb_3Sn *Proc. SRF'21* (*Int. Conf. on RF Superconductivity*) (*Geneva, Switzerland*) (JACoW Publishing) pp 516–21
[37] Kubo T 2022 Effects of nonmagnetic impurities and subgap states on the kinetic inductance, complex conductivity, quality factor and depairing current density *Phys. Rev. Appl.* **17** 014018
[38] Zhang R, Gao P and Wang X 2017 Strain dependence of critical superconducting properties of Nb_3Sn with different intrinsic strains based on a semi-phenomenological approach *Cryogenics* **86** 30–37
[39] Henry M D, Wolfley S, Monson T, Clark B G, Shaner E and Jarecki R 2014 Stress dependent oxidation of sputtered niobium and effects on superconductivity *J. Appl. Phys.* **115** 083903
[40] Guritanu V, Goldacker W, Bouquet F, Wang Y, Lortz R, Goll G and Junod A 2004 Specific heat of Nb_3Sn: The case for a second energy gap *Phys. Rev. B* **70** 184526
[41] Aull S K 2023 The potential of energetic condensation techniques for SRF applications: the first extensive SRF performance study on Nb/Cu by ECR deposition *Phd Thesis* University of Siegen
[42] Keckert S *et al* 2019 Critical fields of Nb_3Sn prepared for superconducting cavities *Supercond. Sci. Technol.* **32** 075004
[43] Leith S 2024 Nb3Sn/Cu — Status and Perspectives Invited Seminar Talk (VSC Seminar Series)
[44] Keckert S, Hall D L, Knobloch J, Kugeler O and Liepe M 2018 Surface resistance characterization of Nb_3Sn using the HZB quadrupole resonator *Proc. Int. Conf. on RF Superconductivity (SRF'17)* (*China, 2017*) vol 18 (JACoW Publishing) pp 863–6
[45] Fonnesu D 2024 Nb_3Sn films on Cu by Magnetron Sputtering for SRF cavities at INFN-LNL *11th International Workshop on Thin Films and New Ideas for Pushing the Limits of RF Superconductivity (Tfsrf2024), Bat* vol 100 (Université Paris-Saclay)
[46] Als-Nielsen J and McMorrow D 2011 *Elements of Modern X-ray Physics* (Wiley) (https://doi.org/10.1002/9781119998365)
[47] Castaing R 1952 Application des sondes électroniques à une méthode d'analyse ponctuelle chimique et cristallographique These Universite de Paris
[48] Kanaya K A and Okayama S 1972 Penetration and energy-loss theory of electrons in solid targets *J. Phys. D: Appl. Phys.* **5** 43
[49] Fonnesu D *et al* 2023 Influence of the coating parameters on the T_c of Nb_3Sn thin films on copper deposited via DC magnetron sputtering *21st Int. Conf. on RF Superconductivity (SRF2023)* (*Grand Rapids, MI, USA*) (JACoW Publishing) (https://doi.org/10.18429/JACoW-SRF2023-MOPMB013)
[50] Zhu L, Lu X, Xiao L and Xie D 2022 The effect of thickness of niobium isolation layer on properties of copper-based Nb_3Sn films *Nucl. Instrum. Methods Phys. Res. A* **1042** 167417